Electronic Supplementary Material (ESI) for Inorganic Chemistry Frontiers.

Supporting information

Synergistic Role of Hydrogen bond and Band degeneracy Leads to Enhanced X-ray Detection in HPIP-$(NH_4)_{0.7}Cs_{0.3}Br_3 \cdot H_2O$ Perovskites

Pengxiang Dong[†, ‡], Chensheng Lin[†], Xin Zhao[†], Yicong Lv[†], Ning Ye[§] and Min Luo[,†]*

†Key Laboratory of Optoelectronic Materials Chemistry and Physics, Fujian Institute of Research on the Structure of Matter, Chinese Academy of Sciences, Fuzhou, Fujian 350002, China.

‡School of Physical Science and Technology, ShanghaiTech University, Shanghai, 201210, China.

§Tianjin Key Laboratory of Functional Crystal Materials, Institute of Functional Crystal, Tianjin University of Technology, Tianjin, 300384, China.

E-mail: lm8901@fjirsm.ac.cn

Keywords: molecular perovskite, X-ray detection, Cs-Incorporated, Orbital Degeneracy.

Experimental:

Materials preparation: Ammonium bromide (NH_4Br,99%), Cesium bromide (CsBr,99%), Hydrobromic acid (HBr) (40%), and Homopiperazine (HPIP,99%) were purchased from Adamas Reagent. we confirmed that all the reagents and chemicals were used as received without further purification.

Synthesis of HPIP-XBr_3 H_2O powders: HPIP (10.008 g, 100 mmol), XBr (100 mmol), and HBr(40%, 50 mL) are dissolved in 80 ml H_2O and stirred at room temperature for 12 h. Then, the mixed solution was evaporated using a rotary evaporator at 60°C, then the white product was cleaned with ethanol three times. Finally, the white product was dried for 24 hours at 50°C in a vacuum oven.

Synthesis of HPIP-XBr_3 H_2O SCs: The HPIP-XBr_3 H_2O SCs were grown by dissolving the HPIP-XBr_3 H_2O powders into the H_2O to form a saturated solution. Then, the impurities in the mixture solution were removed by filter, and transferred into a crystallizing dish for holding at a constant temperature (35°C) in the oven for several days to obtain HPIP-XBr_3 H_2O single crystals.

Single-Crystal Structure Determination: Single-crystal X-ray diffraction (SC-XRD) data were performed on a Rigaku Mercury CCD diffractometer equipped with graphite-monochromatic Cu-Kα radiation (λ = 1.54184Å) and Mo-Kα radiation (λ = 0.7103Å). The crystal structure of HPIP-XBr_3 H_2O was solved by using the ShelXT and then refined by the ShelXL on OLEX2 package1, 2. The program PLATON2 was used to check for the structure. Crystallographic data and structure refinements of HPIP-XBr3 H2O were given in Table S3.

Powder X-ray diffraction (PXRD): The PXRD data of HPIP-XBr_3 H_2O were measured on a Miniflex600 powder X-ray diffractometer with Cu Kα radiation (λ = 1.54184 Å) in the 2θ range from 10 to 60°.

Nuclear Magnetic Resonance (NMR): NMR was performed using AVANCE III 400 with a frequency of 400 MHz, and deuterated DMSO was used as a solvent.

Energy-dispersive X-ray Spectroscopy Analysis: Microprobe elemental analyses were recorded on a field emission scanning electron microscope (FESEM, SU-8010) with an energy-dispersive X-ray spectroscope (EDS).

Thermal analysis: Thermogravimetric Analysis (TGA) was performed on a Netzsch STA449F3 simultaneous analyzer under flowing N_2 at a rate of 10 °C·min^{-1}.

UV-Vis-NIR Diffuse Reflectance Spectrum and Transmission Spectrum: The UV-Vis-NIR transmission Spectrum of HPIP-NH_4Br_3 H_2O and HPIP-$(NH_4)_{0.7}Cs_{0.3}Br_3$ H_2O were measured on PerkinElmer Lamda950 UV/vis/NIR spectrophotometer. The UV-Vis-NIR Diffuse Reflectance Spectrum of HPIP-$CsBr_3$ H_2O was measured on PerkinElmer Lamda950 UV/vis/NIR spectrophotometer. $BaSO_4$ was used as standard.

First-principles calculations:

All DFT calculations were performed with the CP2K package[1]. We use a Gaussian and augmented

plane waves (GAPW)[2] scheme, in which, the electronic density is expanded in the form of plane waves with a cutoff of 400 Ry. The PBE as the exchange and correlation functional and the core electrons treated as the Geodecker, Teter and Hutter pseudopotentials[3] were used in the calculations. Double-zeta split valance basis sets are used for all atomic kinds. In addition, Grimme's empirical dispersion corrections are also included[4]. The IGHM[5,6] figure is depicted using Multiwfn[7] and VMD software[8].

Device parameters:

Device fabrication preparation for X-ray detector and imager: For the detector, the vacuum evaporation method deposited a thickness of 200 nm Ag electrodes on HPIP-XBr_3 H_2O SCs. The electrode area is 0.0020 cm^2 with a space of 150 μm.

***μτ* product calculation:** In this work, a device structure of Ag/ HPIP-XBr_3 H_2O SCs/Ag was used for photoconductivity measurement. Then, the simplified Hecht equation was utilized to extract the μτ product from photoconductivity curves, as follows:

$$I = \frac{I_0 \mu \tau V}{d^2}\left[1 - exp\left(-\frac{d^2}{\mu \tau V}\right)\right]$$

where I_0 is the saturated photoinduced current, V is the bias voltage, and d is the device thickness.

Gain factor calculation: The gain factor can be calculated as follows:[9]

$$Gain\ factor = \frac{I_R}{I_P}$$

where I_R and I_P stand for induced photocurrent and theoretical photocurrent under X-ray illumination. $I_R$can be obtained in the experiment, while I_P should calculate as $I_P = \varphi \beta e$.
The φ (photon absorption rate) is defined as:

$$\varphi = \frac{\epsilon D\, m_s}{E_{ph}}$$

where β (the number of excited carriers per X-ray photon) is defined as $\beta = \frac{E_{Ph}}{W \pm}$ Notably, e represents electric charge, ε the fraction of photons in the sample (typically defined as 1), D the dose rate, ms the mass of the sample and E_{Ph} X-ray energy. $W\pm$ is the e-h pair creation energy, which is calculated by $W\pm = 1.43 + 2Eg$.

Signal-to-noise ratio (SNR) calculation: The SNR is calculated according to the relation: $SNR=I_{signal}/I_{noise}$, where the signal current (I_{signal}) is the difference between the average photocurrent (I_{photo}) and the average dark current (I_{dark}), and the noise current (I_{noise}) is obtained by calculating the standard deviation of the photocurrent.

Dark current drift (D) calculation: The D is calculated according to the relation $D=|J_{finish}-J_{begin}|/(t\times E)$, where t is duration, E is applied electric field, J_{finish} and J_{begin} represent current density at the end and beginning, respectively.

X-ray detectors: The X-ray detection measurements were performed on a modified Super Nova instrument. The X-ray is generated by a tungsten anode tube and is operated with a constant 40 keV

acceleration voltage. Operational current can be easily tuned from 5 to 40 μA to adjust the emitted X-ray dose rate. All the X-ray response characterization was conducted in a dark ambient atmosphere by dark curtain, the photocurrent was recorded by a high-precision electrometer (Keithley 6517B). All measurements were performed at room temperature.

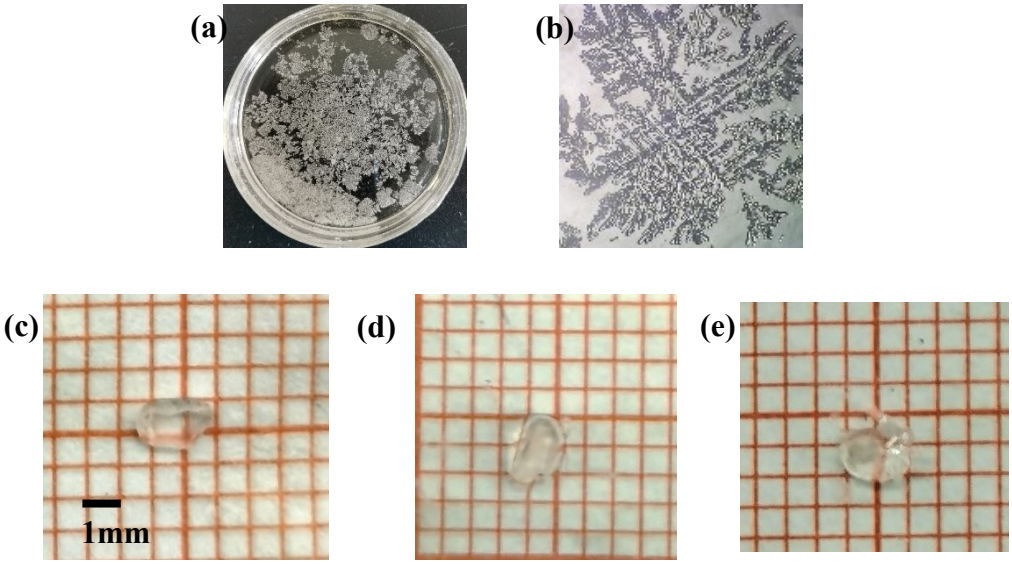

Figure S1. (a) Optical photo and (b) microscope photo of dendrites grown by HPIP^{-}CsBr$_3$. (c) Optical photo of HPIP^{-}CsBr$_3$ SC and placed in the natural environment for (d) 3 days and (e) 7 days.

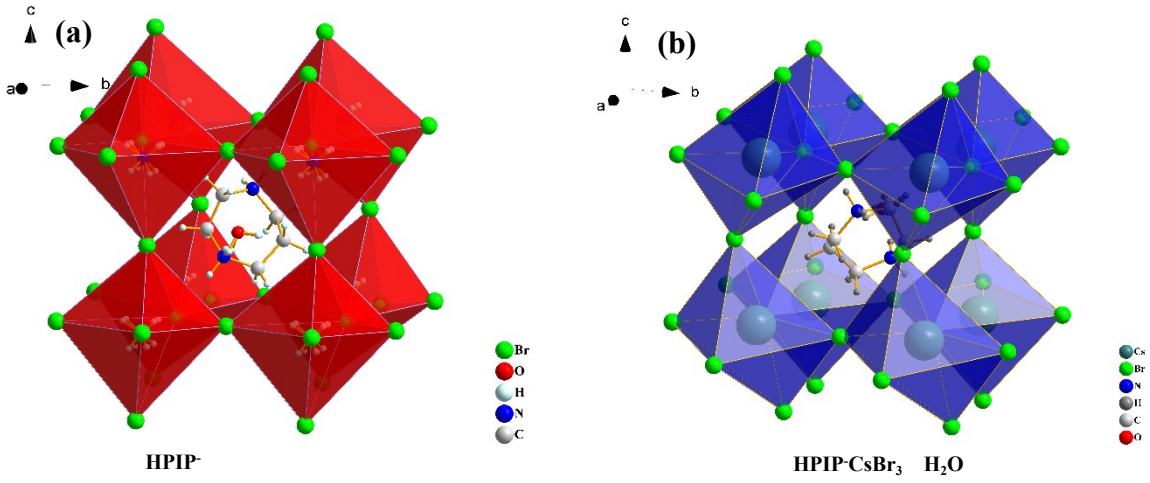

Figure S2. Crystal structure of (a) HPIP^{-}NH$_4$Br$_3$ H$_2$O and (b) HPIP^{-}CsBr$_3$ H$_2$O.

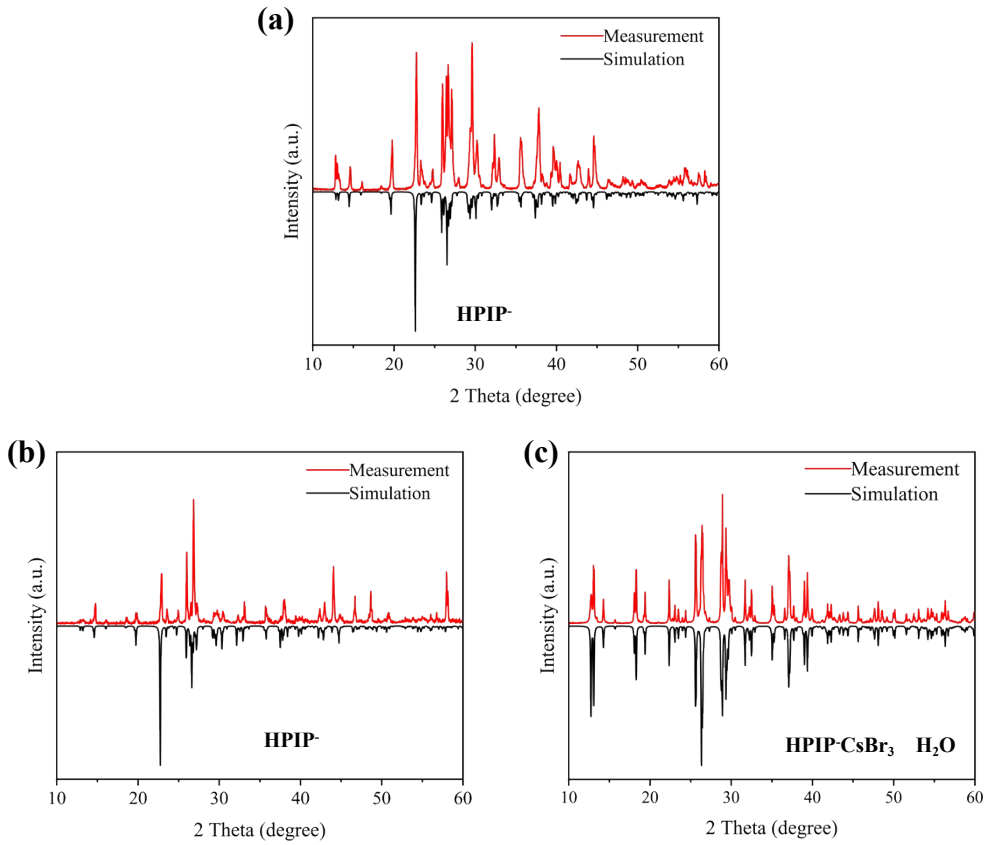

Figure S3. Calculated and experimental powder X-ray diffraction patterns of (a) HPIP$^-$ $(NH_4)_{0.7}Cs_{0.3}Br_3$ H_2O, (b) HPIP$^-NH_4Br_3$ H_2O, and (c) HPIP$^-CsBr_3$ H_2O.

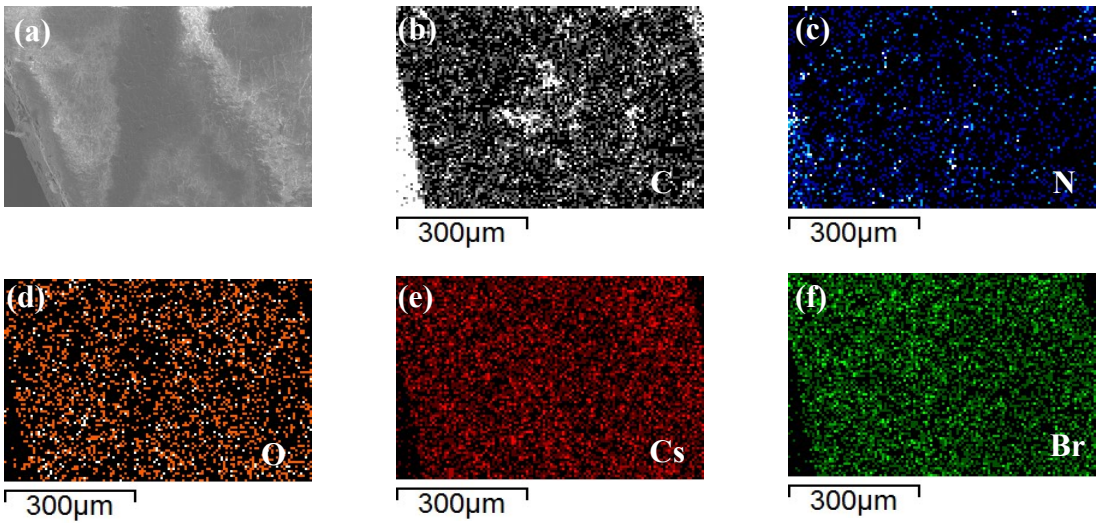

Figure S4. Element analysis of HPIP$^-(NH_4)_{0.7}Cs_{0.3}Br_3$ H_2O SC: (a) SEM images and (b-f) the energy-dispersive spectrometric mapping.

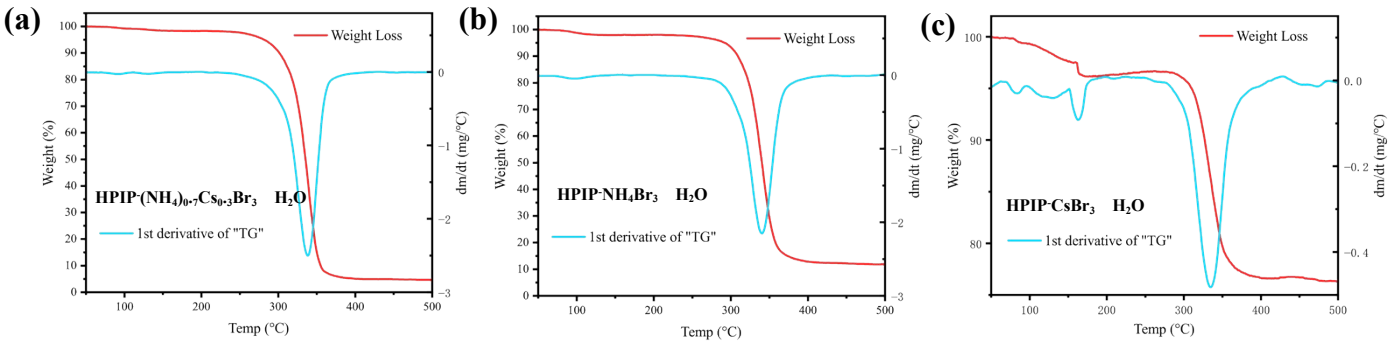

Figure S5. TG characterization of (a) HPIP-$(NH_4)_{0.7}Cs_{0.3}Br_3$ H_2O, (b) HPIP-NH_4Br_3 H_2O, and (c) HPIP-$CsBr_3$ H_2O.

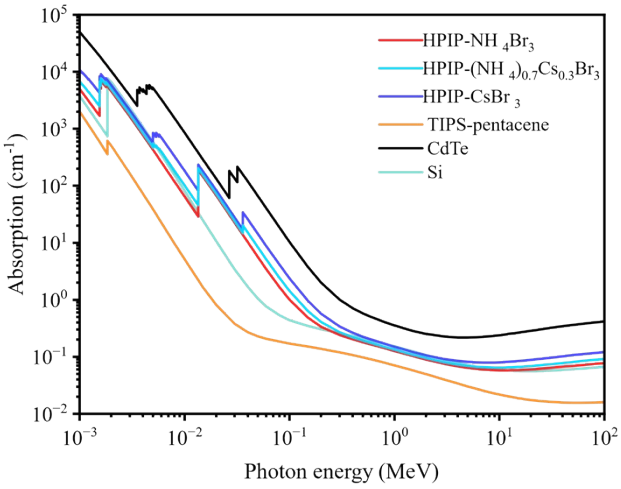

Figure S6. Absorption coefficients of HPIP-$CsBr_3$ H_2O, CdTe, TIPS-pentacene, and Si over a wide range of photon energies.

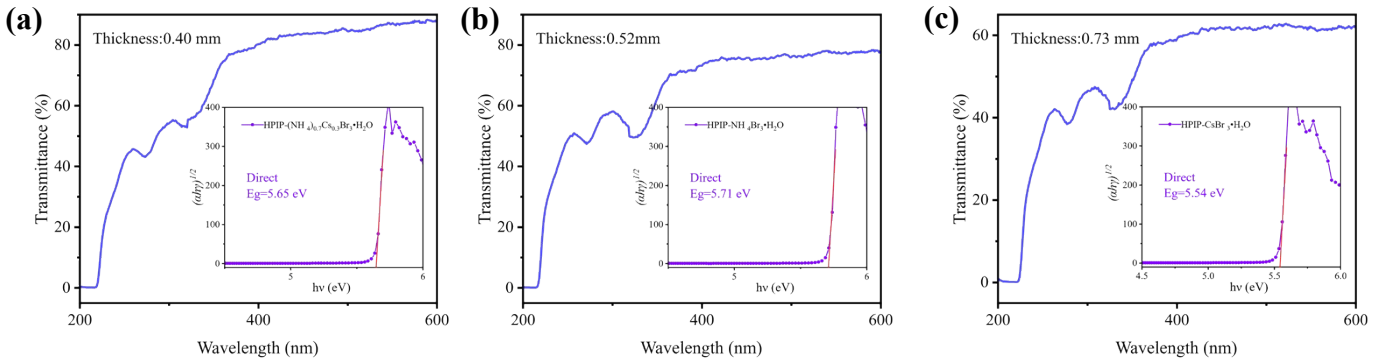

Figure S7. The transmittance spectrum and Tauc plot for an indirect band gap of (a) HPIP-$(NH_4)_{0.7}Cs_{0.3}Br_3$ H_2O, (b) HPIP-NH_4Br_3 H_2O, and (c) HPIP-$CsBr_3$ H_2O.

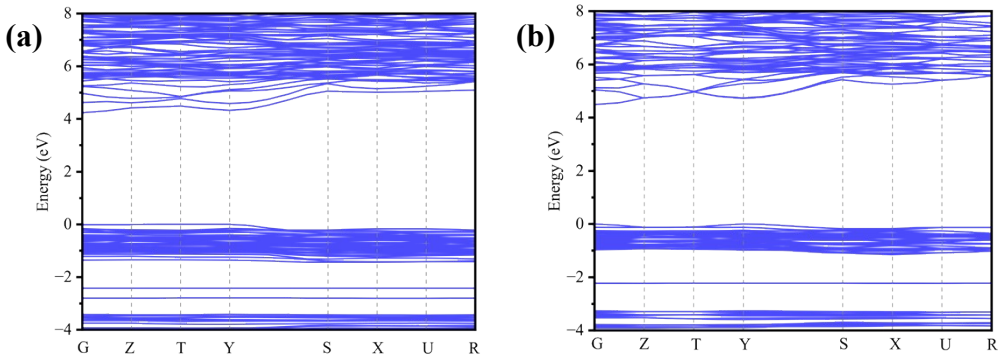

Figure S8. The band gap of (a) HPIP-NH_4Br_3 H_2O and (b) HPIP-$CsBr_3$ H_2O.

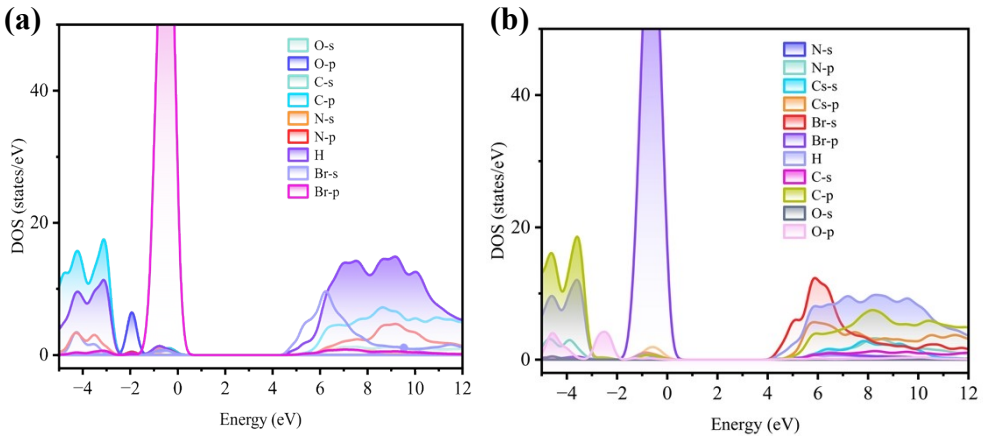

Figure S9. Electronic density of states for HPIP-NH_4Br_3 H_2O: (a) HPIP-NH_4Br_3 H_2O, and (b) HPIP-$CsBr_3$ H_2O.

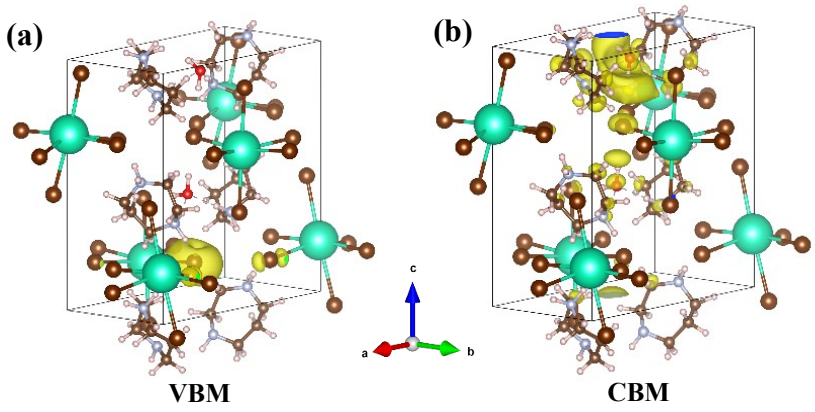

Figure S10. Band nature of HPIP-$CsBr_3$ H_2O: the charge-density distributions for (a) VBM and (b) CBM.

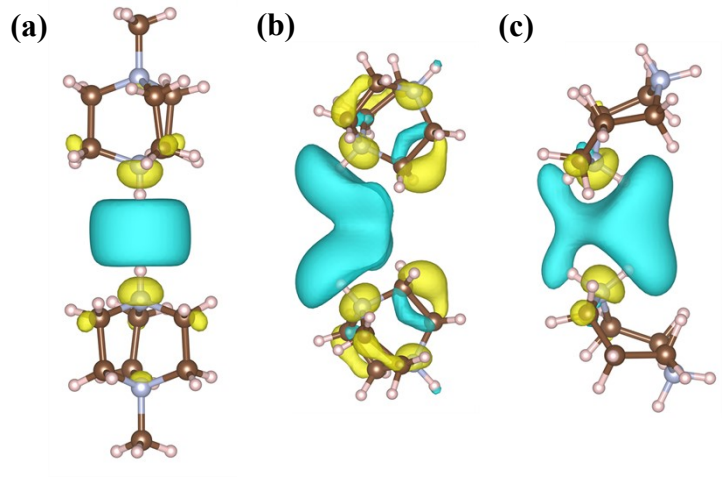

Figure S11. The lowest unoccupied molecular orbital between a) MDABCO, b) DABCO and c) HPIP molecules.

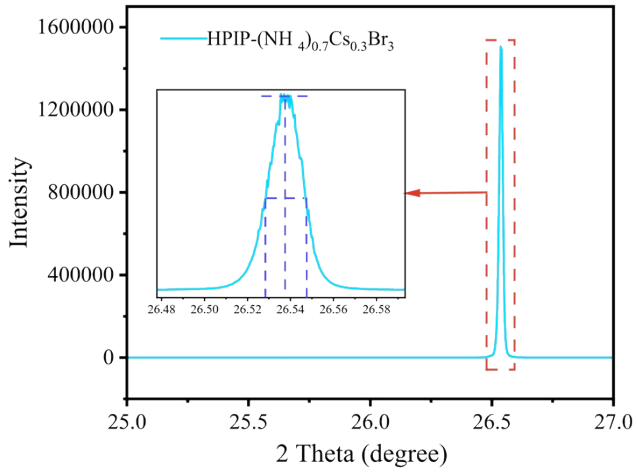

Figure S12 X-ray rocking curve of the HPIP-$(NH_4)_{0.7}Cs_{0.3}Br_3$•H_2O crystal

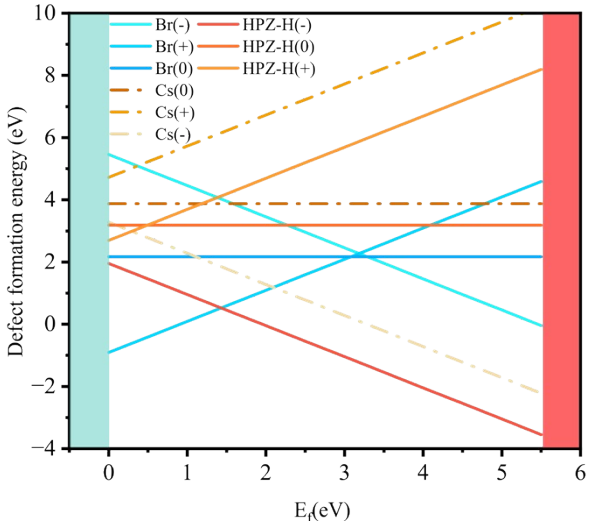

Figure S13. The defect formation energy of HPIP·$CsBr_3$ H_2O with different components.

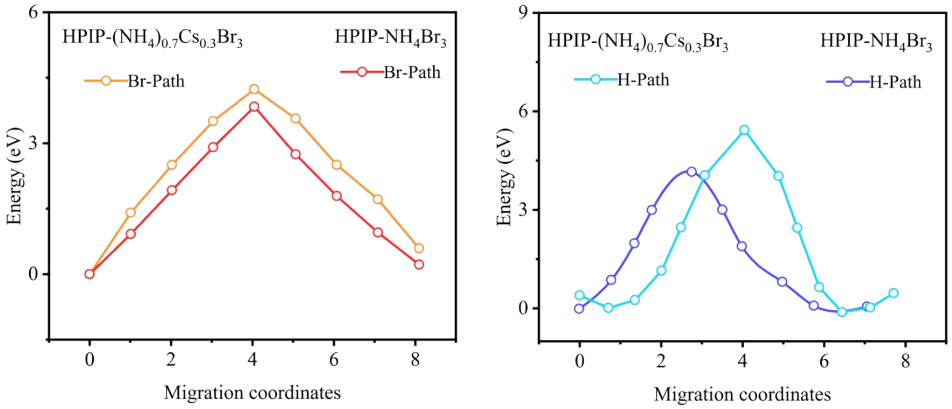

Figure S14 Ionic migration energy of Br and H ions in NH_4/Cs and NH_4-based crystals

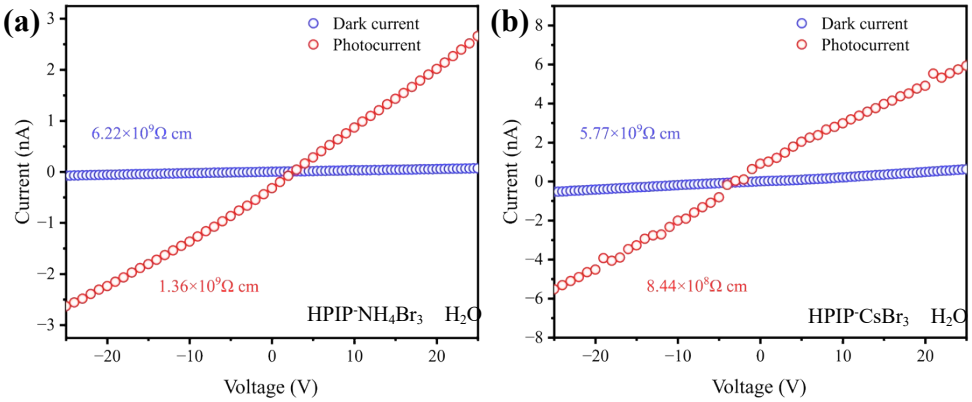

Figure S15. The resistivity of (a) HPIP-NH_4Br_3 H_2O, and (b) HPIP-$CsBr_3$ H_2O.

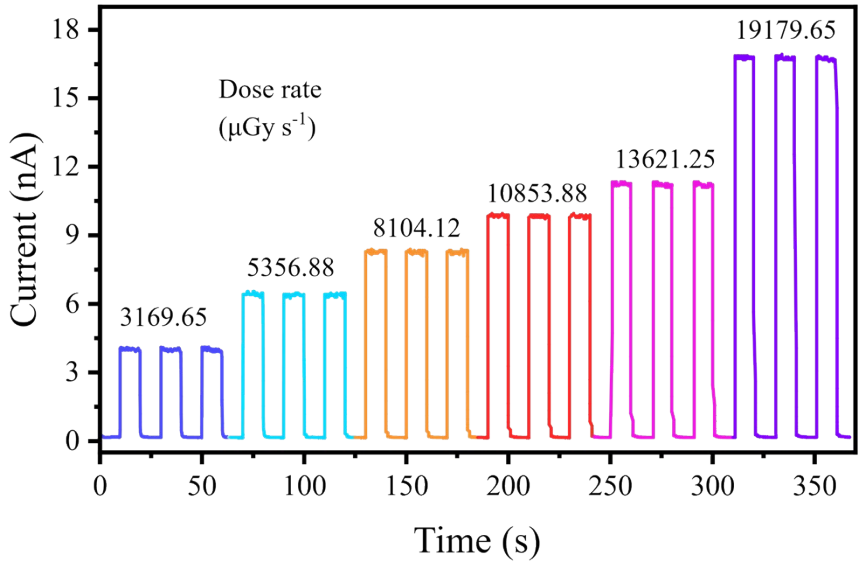

Figure S16. Photocurrent response versus time under different dose rates.

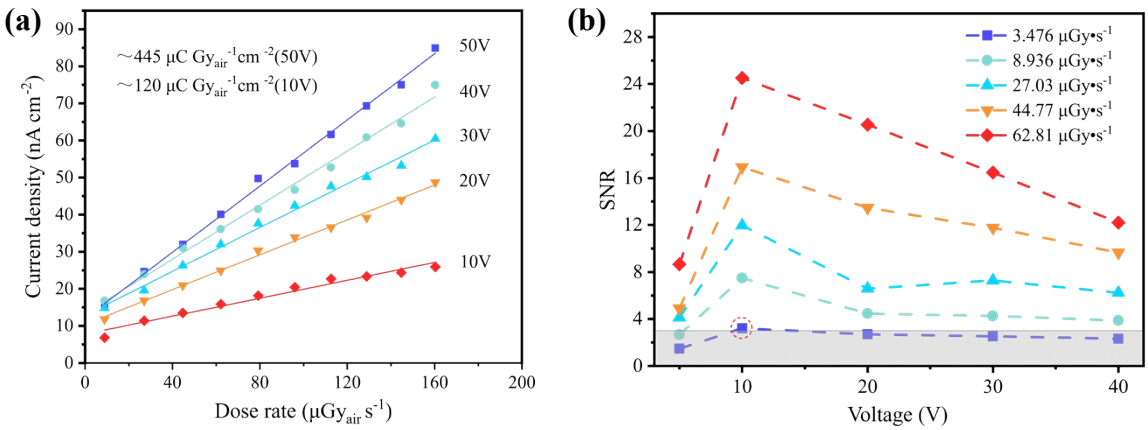

Figure S17. Device performance of HPIP-NH_4Br_3 H_2O SC-based device: (a) X-ray response of photocurrent under different bias and (b) Signal-to-noise ratio (SNR) of the device under a series of bias voltages on exposure to different dose rates.

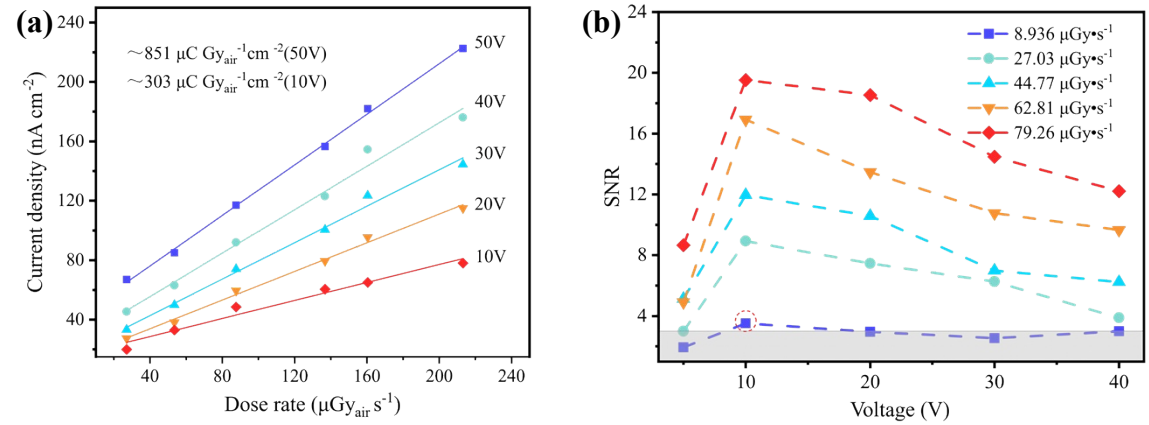

Figure S18. Device performance of HPIP-$CsBr_3$ H_2O SC-based device: (a) X-ray response of photocurrent under different bias and (b) Signal-to-noise ratio (SNR) of the device under a series of bias voltages on exposure to different dose rates.

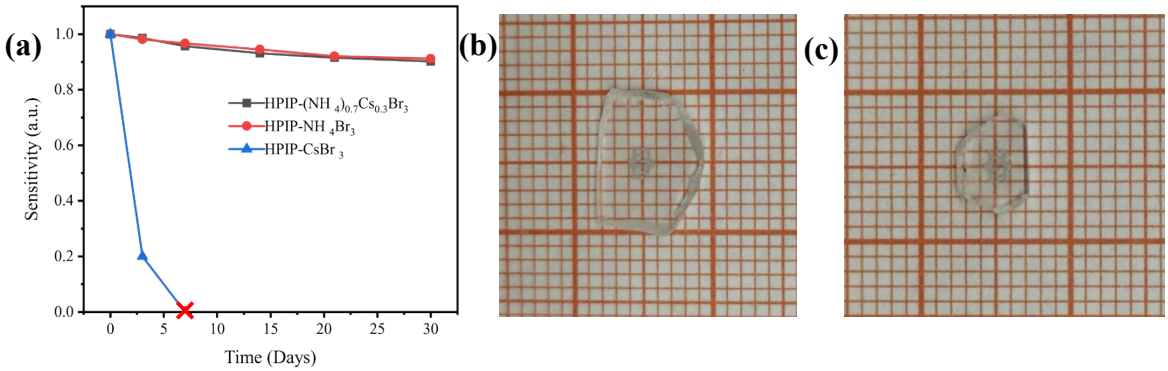

Figure S19. a) The long-term stability of X-ray detector under environmental conditions for 30 days. Photo of the (b) HPIP-$(NH_4)_{0.7}Cs_{0.3}Br_3$ H_2O single crystal and (c) HPIP-NH_4Br_3 H_2O single crystal under environmental conditions after 30 days.

Table S1. Crystal Data and Structure Refinement of HPIP-XBr_3 H_2O

Compound	HPIP-NH_4Br_3 H_2O	HPIP-$(NH_4)_{0.7}Cs_{0.3}Br_3$ H_2O	HPIP-$CsBr_3$ H_2O
Formula	$(C_5H_{14}N_2)$-NH_4Br_3	$(C_5H_{14}N_2)$-$(NH_4)_{0.7}Cs_{0.3}Br_3$	$(C_5H_{14}N_2)$-$CsBr_3$
Formula weight	372.99	405.64	967.66
Temperature	287.15 K	293(2) K	297.15 K
Wavelength	0.71073 A	1.54184 A	0.71073 A
Crystal system	Orthorhombic	Orthorhombic	Orthorhombic
space group	Pmc2(1)	Pmc2(1)	Pmc2(1)
Unit cell	a = 13.3845(9) Å α=90° b = 6.7534(5) Å β=90° c = 13.7252(9) Å γ=90°	a = 13.4298(3) Å α=90° b = 6.81540(10) Å β=90° c = 13.7663(3) Å γ=90°	a = 13.5281(5) Å α=90° b = 6.9306(2) Å β=90° c = 13.9050(5) Å γ=90°
Volume(Å^3)	1240.63(15)	1260.02(4)	1303.70(8)
Z	4	4	2
Calculated density	1.997 g/cm^3	2.138 g/cm^3	2.465 g/cm^3
F(000)	732	778	892
GOF on F^2	0.976	1.068	1.048
R/wR (I>2 σ(I))	R_1 = 0.0430, wR_2 = 0.0925	R_1 = 0.0567, wR_2 = 0.1484	R_1 = 0.0206, wR_2 = 0.0428
R/wR (all data)	R_1 = 0.0580, wR_2 = 0.0966	R_1 = 0.0572, wR_2 = 0.1495	R_1 = 0.0251, wR_2 = 0.0438

[a] $R(F) = \Sigma||F_o| - |F_c||/\Sigma|F_o| \cdot wR(F_o^2) = [\Sigma w(F_o^2 - F_c^2)^2 / \Sigma w(F_o^2)^2]$[10]

Table S2. Summary of Br-Br and Br-X bond lengths.

HPIP-NH_4Br_3 H_2O		HPIP-$(NH_4)_{0.7}Cs_{0.3}Br_3$ H_2O		HPIP-$CsBr_3$ H_2O	
label	Distances (Å)	label	Distances (Å)	label	Distances (Å)
Br01-Br02	5.544	Br03-Br01	5.572	Br3-Br4	4.034
Br02-Br01	5.46	Br01-Br03	5.542	Br1-Br	4.275
Br04-Br03	5.294	Br04-Br02	5.337	Br-Br3	4.394
Br02-Br04	5.287	Br03-Br04	5.328	Br4-Br3	4.486
Br03-Br05	5.203	Br01-Br04	5.268	Br1-Br2	4.514
Br04-Br01	5.195	Br02-Br05	5.224	Br2-Br	4.677
Br04-Br05	5.123	Br04-Br05	5.124	Br4-Br	4.734
Br03-Br05	4.953	Br05-Br02	4.972	Br2-Br1	4.836
Br05-Br03	4.719	Br05-Br02	4.755	Br1-Br2	5.045
Br04-Br02	4.636	Br03-Br04	4.67	Br-Br2	5.183
Br04-Br05	4.593	Br05-Br04	4.609	Br1-Br2	5.269
Br03-Br05	4.416	Br02-Br05	4.455	Br4-Br	5.384
Br01-Br02	4.4	Br03-Br01	4.421	Br3-Br	5.392
Br01-Br04	4.399	Br04-Br01	4.411	Br-Br1	5.49
Br03-Br04	4.278	Br02-Br04	4.277	Br3-Br4	5.65
Br01-Br02	4.04	Br01-Br03	4.036	Br4-Br3	5.682
N00A-Br02	3.606	N|Cs06-Br03	3.63	Cs00-Br1	3.46
Br02-N00A	3.503	N|Cs06-Br03	3.515	Cs1-Br3	3.465
Br05-N007	3.459	N|Cs06-Br04	3.497	Cs1-Br3	3.475
Br04-N00A	3.458	N|Cs06-Br04	3.497	Br2-Cs00	3.479

Br04-N00A	3.458	N00|Cs00-Br02	3.468	Cs00-Br2	3.485
N007-Br04	3.454	N00|Cs00-Br05	3.464	Br1-Cs00	3.503
Br04-N007	3.454	N00|Cs00-Br04	3.454	Cs00-Br	3.511
Br03-N007	3.429	Br04-N00|Cs00	3.454	Cs00-Br	3.511
N007-Br05	3.414	N00|Cs00-Br05	3.431	Br-Cs1	3.522
Br01-N00A	3.398	N|Cs06-Br01	3.428	Cs1-Br	3.522
N007-Br03	3.367	Br01-N|Cs06	3.396	Br4-Cs1	3.598
N00A-Br01	3.36	N00|Cs00-Br02	3.379	Cs1-Br4	3.642

Table S3. Summary of Br-X-Br bond angles.

$HPIP^{-}NH_4Br_3$ H_2O		$HPIP^{-}(NH_4)_{0.7}Cs_{0.3}Br_3$ H_2O		$HPIP^{-}CsBr_3$ H_2O	
label	angles (º)	label	angles (º)	label	angles (º)
Br(01)-N(00A)-Br(01)	174.0(6)	Br(01)-N|Cs(06)-Br(01)	174.30(11)	Br(1)-Cs(00)-Br(1)	168.94(3)
Br(01)-N(00A)-Br(02)	79.6(3)	Br(01)-N|Cs(06)-Br(04)	99.68(4)	Br(1)-Cs(00)-Br	103.907(12)
Br(01)-N(00A)-Br(02)	106.4(5)	Br(01)-N|Cs(06)-Br(04)	79.15(4)	Br(1)-Cs(00)-Br	75.094(12)
Br(01)-N(00A)-Br(02)	70.7(9)	Br(01)-N|Cs(06)-Br(04)	99.68(4)	Br(1)-Cs(00)-Br	103.907(12)
Br(01)-N(00A)-Br(02)	105.3(8)	Br(01)-N|Cs(06)-Br(04)	79.15(4)	Br(1)-Cs(00)-Br	75.094(12)
Br(01)-N(00A)-Br(04)	99.2(3)	Br(04)-N|Cs(06)-Br(04)	148.65(10)	Br(1)-Cs(00)-Br(2)	93.18(2)
Br(01)-N(00A)-Br(04)	79.5(3)	Br(01)-N|Cs(06)-Br(03)	106.59(8)	Br(1)-Cs(00)-Br(2)	88.38(2)
Br(01)-N(00A)-Br(04)	99.2(3)	Br(01)-N|Cs(06)-Br(03)	79.10(6)	Br-Cs(00)-Br	149.28(2)
Br(01)-N(00A)-Br(04)	79.5(3)	Br(04)-N|Cs(06)-Br(03)	98.90(5)	Br(2)-Cs(00)-Br(1)	97.88(2)
Br(04)-N(00A)-Br(02)	99.3(3)	Br(04)-N|Cs(06)-Br(03)	98.90(5)	Br(2)-Cs(00)-Br(1)	80.56(2)
Br(04)-N(00A)-Br(02)	81.9(9)	Br(01)-N|Cs(06)-Br(03)	70.05(6)	Br(2)-Cs(00)-Br	95.615(16)
Br(04)-N(00A)-Br(02)	98.8(3)	Br(01)-N|Cs(06)-Br(03)	104.25(8)	Br(2)-Cs(00)-Br	84.001(16)
Br(04)-N(00A)-Br(02)	99.3(3)	Br(04)-N|Cs(06)-Br(03)	81.87(6)	Br(2)-Cs(00)-Br	95.615(16)
Br(02)-N(00A)-Br(02)	176.1(8)	Br(04)-N|Cs(06)-Br(03)	81.87(6)	Br(2)-Cs(00)-Br	84.000(16)
Br(04)-N(00A)-Br(04)	148.8(6)	Br(03)-N|Cs(06)-Br(03)	176.64(8)	Br(2)-Cs(00)-Br(2)	178.438(15)
Br(03)-N(007)-Br(03)	167.2(0)	Br(02)-N|Cs(00)-Br(05)	88.56(10)	Br(3)-Cs(1)-Br(3)	174.18(3)
Br(03)-N(007)-Br(04)	76.8(4)	Br(02)-N|Cs(00)-Br(04)0	102.69(6)	Br(3)-Cs(1)-Br(4)	105.07(2)
Br(03)-N(007)-Br(04)	76.7(3)	Br(05)-N|Cs(00)-Br(04)0	84.02(8)	Br(3)-Cs(1)-Br(4)	69.11(2)
Br(03)-N(007)-Br(04)	101.1(1)	Br(02)-N|Cs(00)-Br(04)1	102.69(6)	Br(3)-Cs(1)-Br(4)	107.11(2)
Br(03)-N(007)-Br(04)	101.8(0)	Br(05)-N|Cs(00)-Br(04)1	84.02(8)	Br(3)-Cs(1)-Br(4)	78.71(2)
Br(03)-N(007)-Br(05)	93.8(2)	Br(04)0-N|Cs(00)-Br(04)	151.57(13)	Br(3)-Cs(1)-Br	101.019(12)
Br(03)-N(007)-Br(05)	98.9(6)	Br(02)-N|Cs(00)-Br(05)	93.21(10)	Br(3)-Cs(1)-Br	77.800(12)
Br(03)-N(007)-Br(05)	79.7(4)	Br(05)-N|Cs(00)-Br(05)	178.23(12)	Br(3)-Cs(1)-Br	77.800(12)
Br(03)-N(007)-Br(05)	87.4(5)	Br(04)0-N|Cs(00)-Br(05)	95.58(8)	Br(3)-Cs(1)-Br	101.019(12)
Br(04)-N(007)-Br(05)	96.4(5)	Br(04)1-N|Cs(00)-Br(05)	95.58(8)	Br(4)-Cs(1)-Br(4)	176.218(18)
Br(04)-N(007)-Br(05)	96.4(5)	Br(02)-N|Cs(00)-Br(02)	168.99(16)	Br-Cs(1)-Br(4)	98.247(16)
Br(04)-N(007)-Br(05)	83.2(7)	Br(05)-N|Cs(00)-Br(02)	80.43(10)	Br-Cs(1)-Br(4)	98.247(16)
Br(04)-N(007)-Br(05)	83.2(7)	Br(04)0-N|Cs(00)-Br(02)	76.31(6)	Br-Cs(1)-Br(4)	82.702(16)
Br(05)-N(007)-Br(05)	178.7(1)	Br(04)1-N|Cs(00)-Br(02)	76.31(6)	Br-Cs(1)-Br(4)	82.702(16)
Br(04)-N(007)-Br(04)	152.1(6)	Br(05)0-N|Cs(00)-Br(02)	97.81(11)	Br-Cs(1)-Br	147.10(3)

Table S4. Ion radius in the $HPIP^{-}XBr_3$ H_2O.

Ions	$HPIP^{2+}$	$NH4^{+}$	Cs^{+}	Br^{-}
Radius (pm)	241	146	168	196

Table S5. Calculated Goldschmidt Tolerance Factor (t) for $HPIP^{-}XBr_3$ H_2O

Compound	$HPIP^{-}NH_4Br_3$	$HPIP^{-}(NH_4)_{0.7}Cs_{0.3}Br_3$	$HPIP^{-}CsBr_3$
t	0.91	0.89	0.84

Table S6. Summary of the X-ray detection performance of several single crystal-based detectors.

Materials	**Sensitivity**	**Detection limit**	**Ref.**
$MA_3Bi_2I_9$	1947 $\mu C \cdot Gyair^{-1} \cdot cm^{-2}$ at 60 $V \bullet mm^{-1}$	83 $nGy \cdot s^{-1}$	[11]
$MA_3Bi_2I_9$	10620 $\mu C \cdot Gyair^{-1} \cdot cm^{-2}$ at 48 $V \bullet mm^{-1}$	N/A	[12]
$Rb_3Bi_2I_9$	159.7 $\mu C \cdot Gyair-1 \cdot cm-2$ at 300 $V \bullet mm^{-1}$	8.32 $nGy \cdot s^{-1}$	[13]
$MAPbBr_3$ with MoO_3	2552 $\mu C \cdot Gyair^{-1} \cdot cm^{-2}$ 4.5 $V \bullet mm^{-1}$	N/A	[14]
$MA_xCs_{1-x}PbBr_3$	2017 $\mu C \cdot Gyair^{-1} \cdot cm^{-2}$ at 0.5 $V \bullet mm^{-1}$	1200 $nGy \cdot s^{-1}$	[15]
Cuboid $MAPbI_3$	968.9 $\mu C \cdot Gyair^{-1} \cdot cm^{-2}$ at 1 $V \bullet mm^{-1}$	N/A	[16]
$FAPbBr_3$	130 $\mu C \cdot Gyair^{-1} \cdot cm^{-2}$ at 0.5 $V \bullet mm^{-1}$	300 $nGy \cdot s^{-1}$	[17]
DABCO-NH_4Br_3	173-176 $\mu C \cdot Gyair^{-1} \cdot cm^{-2}$ at 1250 $V \bullet mm^{-1}$	4960 $nGy \cdot s^{-1}$	[18]
DABCO-NH_4Cl_3	165 $\mu C \cdot Gyair^{-1} \cdot cm^{-2}$ at 1250 $V \bullet mm^{-1}$	N/A	[18]
DABCO-NH_4I_3	567 $\mu C \cdot Gyair^{-1} \cdot cm^{-2}$ at 1250 $V \bullet mm^{-1}$	N/A	[18]
MDABCO-NH_4I_3	1997 ± 80 $\mu C \cdot Gyair^{-1} \cdot cm^{-2}$ at 1250 $V \bullet mm^{-1}$	N/A	[19]
DABCO-$CsBr_3$	1345 $\mu C \cdot Gyair^{-1} \cdot cm^{-2}$ at 5000 $V \bullet mm^{-1}$	445 $nGy \cdot s^{-1}$	[20]
MDABCO-$NH_4(PF_6)_3$	2078 $\mu C \cdot Gyair^{-1} \cdot cm^{-2}$ at 330 $V \bullet mm^{-1}$	16.3 $nGy \cdot s^{-1}$	[21]
DABCO-$N_2H_5Br_3$	1142±10.3 $\mu C \cdot Gyair^{-1} \cdot cm^{-2}$ at 200 $V \bullet mm^{-1}$	2680 $nGy \cdot s^{-1}$	[22]
DABCO-$N_2H_5I_3$	1186±9.6 $\mu C \cdot Gyair^{-1} \cdot cm^{-2}$ at 200 $V \bullet mm^{-1}$	2880 $nGy \cdot s^{-1}$	[22]
$HPIP^{-}NH_4Br_3$ H_2O	445 $\mu C \cdot Gyair^{-1} \cdot cm^{-2}$ at 333 $V \bullet mm^{-1}$	3476 $nGy \cdot s^{-1}$	
$HPIP^{-}CsBr_3$ H_2O	874 $\mu C \cdot Gyair^{-1} \cdot cm^{-2}$ at 333 $V \bullet mm^{-1}$	8920 $nGy \cdot s^{-1}$	**This Work**
$HPIP^{-}(NH_4)_{0.7}Cs_{0.3}Br_3$ H_2O	1661 $\mu C \cdot Gyair^{-1} \cdot cm^{-2}$ at 333 $V \bullet mm^{-1}$	402 $nGy \cdot s^{-1}$	

References

[1] J. VandeVondele, M. Krack, F. Mohamed, M. Parrinello, T. Chassaing, J. Hutter, *Comput. Phys. Commun.* **2005**, *167*, 103.

[2] M. Iannuzzi, J. Hutter, *Phys. Chem. Chem. Phys.* **2007**, *9*, 1599.

[3] S. Goedecker, M. Teter, J. Hutter, *Phys. Rev. B* **1996**, *54*, 1703.

[4] E. R. Johnson, S. Keinan, P. Mori-Sánchez, J. Contreras-García, A. J. Cohen, W. Yang, *J. Am. Chem. Soc.* **2010**, *132*, 6498.

[5] T. Lu, Q. Chen, *J. Comput. Chem.* **2022**, *43*, 539.

[6] S. Grimme, J. Antony, S. Ehrlich, H. Krieg, *J. Chem. Phys.* **2010**, *132*, 154104.

[7] T. Lu, F. Chen, *J. Comput. Chem.* **2012**, *33*, 580.

[8] W. Humphrey, A. Dalke, K. Schulten, *J. Mol. Graph.* **1996**, *14*, 33.

[9] W. Pan, H. Wu, J. Luo, Z. Deng, C. Ge, C. Chen, X. Jiang, W.-J. Yin, G. Niu, L. Zhu, L. Yin, Y. Zhou, Q. Xie, X. Ke, M. Sui, J. Tang, *Nat. Photonics* **2017**, *11*, 726.

[10] G. M. Sheldrick, *Acta Crystallogr. A* **2008**, *64*, 112.

[11] Y. Liu, Z. Xu, Z. Yang, Y. Zhang, J. Cui, Y. He, H. Ye, K. Zhao, H. Sun, R. Lu, M. Liu, M. G. Kanatzidis, S. (Frank) Liu, *Matter* **2020**, *3*, 180.

[12] X. Zheng, W. Zhao, P. Wang, H. Tan, M. I. Saidaminov, S. Tie, L. Chen, Y. Peng, J. Long, W.-H. Zhang, *J. Energy Chem.* **2020**, *49*, 299.

[13] M. Xia, J. Yuan, G. Niu, X. Du, L. Yin, W. Pan, J. Luo, Z. Li, H. Zhao, K. Xue, X. Miao, J. Tang, *Adv. Funct. Mater.* **2020**, *30*, 1910648.

[14] Z. Fan, J. Liu, W. Zuo, G. Liu, X. He, K. Luo, Q. Ye, C. Liao, *Phys. Status Solidi A* **2020**, *217*, 2000104.

[15] Z. Fan, J. Liu, W. Zuo, G. Liu, X. He, K. Luo, Q. Ye, C. Liao, *Phys. Status Solidi RRL – Rapid Res. Lett.* **2020**, *14*, 2000226.

[16] F. Ye, H. Lin, H. Wu, L. Zhu, Z. Huang, D. Ouyang, G. Niu, W. C. H. Choy, *Adv. Funct. Mater.* **2019**, *29*, 1806984.

[17] M. Yao, J. Jiang, D. Xin, Y. Ma, W. Wei, X. Zheng, L. Shen, *Nano Lett.* **2021**, *21*, 3947.

[18] Q. Cui, X. Song, Y. Liu, Z. Xu, H. Ye, Z. Yang, K. Zhao, S. (Frank) Liu, *Matter* **2021**, *4*, 2490.

[19] X. Song, Q. Li, J. Han, C. Ma, Z. Xu, H. Li, P. Wang, Z. Yang, Q. Cui, L. Gao, Z. Quan, S. (Frank) Liu, K. Zhao, *Adv. Mater.* **2021**, *33*, 2102190.

[20] Q. Cui, N. Bu, X. Liu, H. Li, Z. Xu, X. Song, K. Zhao, S. F. Liu, *Nano Lett.* **2022**, *22*, 5973.

[21] Z. Li, Z. Li, G. Peng, C. Shi, H. Wang, S. Ding, Q. Wang, Z. Liu, Z. Jin, *Adv. Mater.* **2023**, 2300480.

[22] X. Song, H. Cohen, J. Yin, H. Li, J. Wang, Y. Yuan, R. Huang, Q. Cui, C. Ma, S. (Frank) Liu, G. Hodes, K. Zhao, *Small* **2023**, *19*, 2300892.